

# Step-Directed Epitaxy of Unidirectional Hexagonal Boron Nitride on Vicinal Ge(110)

Ju-Hyun Jung, Chao Zhao, Seong-Jun Yang, Jun-Ho Park, Woo-Ju Lee, Su-Beom Song, Jonghwan Kim, Chan-Cuk Hwang, Seung-Hwa Baek, Feng Ding,\* and Cheol-Joo Kim\*

Insulating hexagonal boron nitride (hBN) films with precisely controlled thickness are ideal dielectric components to modulate various interfaces in electronic devices. To achieve this, high-quality hBN with controlled atomic configurations must be able to form pristine interfaces with various materials in devices. However, previously reported large-scale hBN films with uniform thickness either are polycrystalline or are not suitable for atomically clean assembly via mechanical exfoliation, limiting their applications in device technology. Herein, the large-scale growth of monolayer (ML) single crystalline hBN films on Ge(110) substrates by using chemical vapor deposition is reported. Vicinal Ge(110) substrates are used for the step-directed epitaxial growth of hBN, where Ge atomic steps act as the hBN nucleation sites, guiding the unidirectional alignments of multiple hBN domains. Density functional theory calculations reveal that the optimum hydrogen passivations on both hBN edges and Ge surfaces enable the epitaxial coupling between hBN and the Ge step edges and the single crystallinity of the final hBN films. Using epitaxially grown ML hBN films, a few hBN films with controlled stacking orders and pristine interfaces through a layer-by-layer assembly process are fabricated. These films function as high-quality dielectrics to enhance carrier transport in graphene and MoS<sub>2</sub> channels.


## 1. Introduction

Hexagonal boron nitride (hBN), whose surfaces are dangling-bond-free, can serve as an ideal passive buffer layer for high-performance electronic and optoelectronic devices by suppressing unwanted interactions between defect states in the insulator and excited charges in the active channels. The inertness of hBN surfaces enables the formation of pristine van der Waals (vdW) interfaces between hBN and arbitrary materials, thereby improving the device performance greatly.<sup>[1–3]</sup> Additionally, the thickness of the hBN buffer layer can be precisely modulated at the atomic-scale to act as an effective spacer to modulate the interactions between electronic states of constituent materials and the interface. Thereby, advanced devices and material platforms can be realized with desired functionalities, including metallic contacts on two-dimensional (2D) semiconductors with low contact resistance,<sup>[4]</sup> Josephson

J.-H. Jung, S.-J. Yang, J.-H. Park, W.-J. Lee, S.-B. Song, J. Kim, S.-H. Baek, C.-J. Kim  
Center for Van der Waals Quantum Solids  
Institute for Basic Science (IBS) Pohang University of Science and Technology  
Pohang 37673, Republic of Korea  
E-mail: kimcj@postech.ac.kr

J.-H. Jung, J.-H. Park, W.-J. Lee, S.-H. Baek, C.-J. Kim  
Department of Chemical Engineering  
Pohang University of Science and Technology  
Pohang 37673, Republic of Korea

C. Zhao, F. Ding  
Shenzhen Institute of Advanced Electronic Materials, Shenzhen Institute of Advanced Technology  
Chinese Academy of Sciences  
Shenzhen 518103, China  
E-mail: f.ding@siat.ac.cn

 The ORCID identification number(s) for the author(s) of this article can be found under <https://doi.org/10.1002/ssstr.202400297>.

© 2024 The Author(s). Small Structures published by Wiley-VCH GmbH. This is an open access article under the terms of the Creative Commons Attribution License, which permits use, distribution and reproduction in any medium, provided the original work is properly cited.

DOI: 10.1002/ssstr.202400297

C. Zhao, F. Ding  
Faculty of Materials Science and Energy Engineering  
Shenzhen University of Advanced Technology  
Shenzhen 518055, China

C. Zhao, F. Ding  
Shenzhen Institute of Advanced Technology  
Chinese Academy of Sciences  
Shenzhen 518055, China

S.-B. Song, J. Kim  
Department of Materials Science & Engineering  
Pohang University of Science and Technology  
Pohang 37673, Republic of Korea

C.-C. Hwang  
Beamline Research Division  
Pohang Accelerator Laboratory  
Pohang 37673, Republic of Korea

C.-J. Kim  
Institute for Convergence Research and Education in Advanced Technology  
Yonsei University  
Seoul 03722, Republic of Korea

junctions for superconducting circuits with low loss,<sup>[5]</sup> resonant tunnel devices with high operation frequency,<sup>[6]</sup> and excitonic insulators for exciton circuitry.<sup>[7]</sup>

While single-crystalline bulk hBN flakes are mostly used for these purposes, the limited scale of bulk crystals, typically below a few tens of micrometers wide, hampers their widespread application for large-scale arrays of devices. hBN films grown by chemical vapor deposition (CVD) are ideal for large-scale applications, but previous studies have shown either the existence of grain boundaries in the hBN films or interfacial contaminants during the integration process with other active channel materials. These grain boundaries and interfacial contaminants have detrimental effects as trap states on the performance of devices. For instance, the charge carrier mobilities of active channels can be reduced in field-effect transistors (FETs) due to scattering at the trap states, and the quantum yield of light-emitting materials can be lowered due to trap-assisted recombination. The suppression of defect states in hBN becomes even more critical in device applications where electron–electron interactions or electrical currents occur directly across the hBN for device functionalities.<sup>[4–7]</sup>

The seamless stitching of unidirectionally aligned hBN domains grown on a wafer-scale single crystalline metal foil, such as Cu<sup>[8–11]</sup> and Ni,<sup>[12,13]</sup> by CVD approach has been a prevailing method for producing uniform single crystalline hBN films. As revealed in previous computational studies, a zigzag edge of hBN tends to be aligned along a highly symmetric direction of the substrate, which can ensure the epitaxial behavior of hBN growth on a single crystal. If the hBN lattice owns all the symmetric operations of the single crystalline substrate, the crystalline alignment of a hBN domain grown on the substrate cannot be changed by any symmetric operation of the substrate<sup>[13]</sup> and, thus, all the epitaxial hBN islands will be parallelly aligned and finally merged into a large-single crystalline hBN film by seamless stitching. Both experimental<sup>[8–14]</sup> and theoretical<sup>[15]</sup> evidences suggest that these unidirectionally aligned hBN grains on an ultra-flat substrate can be seamlessly stitched together, suppressing the formation of tilt and twin grain boundaries in the hBN film.<sup>[16,17]</sup>

However, hBN films adhered to a metal surface cannot be dry-transferred for clean integration with other device components due to their relatively strong adhesion to metal substrates. This often results in residual contaminants at vdW interfaces after integration, which leads to the in-gap states and the variation of the thickness of hBN spacer. In contrast, hBN films grown on germanium (Ge) surfaces by CVD can be easily dry-exfoliated, allowing for atomically clean assembly.<sup>[18]</sup> Yet, the unidirectionally aligned hBN grains on Ge surfaces have not been realized because of the limited understanding of the mechanism of hBN growth on Ge.<sup>[19]</sup> This hinders the clean integration of hBN with a controlled atomic-scale thickness and minimal defective states. We have included a summary table of key figures of merit for the assembly of hBN from various reports in Table S1, Supporting Information.

In this study, we report the epitaxial growth of unidirectionally aligned monolayer (ML) hBN islands and the seamless stitching of these islands into a single crystalline hBN film on the vicinal Ge(110) surfaces for atomically clean assembly by CVD (Figure 1a). The Ge surface was miscut from the perfect (110)

plane by a specific degree to form parallel atomic steps with controllable step width, which reduces the symmetry of the substrate from the  $C_{2v}$  of the (110) plane to the  $C_s$  or  $C_v$ . The yield of aligned hBN approaches its maximum when the step edge direction of the vicinal surface is parallel to the polar direction of the hBN lattice. Interestingly, the yield of parallel hBN domains changes nonmonotonically when increasing the hydrogen pressure, reaching nearly 100% at an optimized pressure. Our density functional theory (DFT) calculations suggest that hydrogen passivation of both the hBN edge and the substrate is vital for the determination of the hBN orientation on the Ge substrate, demonstrating the importance of the chemical environment for step-directed epitaxial growth of hBN.

## 2. Results and Discussion

### 2.1. Epitaxial Relationship Between hBN and Atomic Steps of Ge

Although, in principle, the formation of atomic steps on the Ge(110) surface can eliminate the inversion symmetry of the substrate and facilitate the unidirectional alignments of grown hBN on the substrate, the most efficient atomic steps for efficient hBN epitaxy have not been identified yet. To investigate the effect of step edge orientation on hBN epitaxy, we grew hBN on two different vicinal Ge(110) substrates, whose miscut directions are toward the [001] and  $[\bar{1}\bar{1}1]$  axes, and we name them as Sub(A) and Sub(B), respectively (Figure 1b,c). X-ray diffraction (XRD) rocking curve measurements using omega ( $\omega$ ) scans (Figure S1, Supporting Information) show that the (110) peaks of the miscut substrates are shifted, confirming that the nominal surfaces have a tilt angle,  $\theta_m$ , with respect to the [110] crystalline orientation (Figure 1d). Atomic force microscopy (AFM) height images reveal that the atomic steps are oriented perpendicular to the miscut direction (Figure S2, Supporting Information). The steps orientations for Sub(A) and Sub(B) are perpendicular to the  $[\bar{1}\bar{1}0]$  and  $[\bar{1}\bar{1}\bar{2}]$  directions of the substrate, respectively.

While the presence of boron (B) and nitrogen (N) elements and B–N chemical bonds were confirmed by X-ray photoelectron spectroscopy (XPS) and Fourier transform infrared spectroscopy (FTIR) on both Sub(A) and Sub(B) (Figure S3, Supporting Information), the grown hBN grains on Sub(A) and Sub(B) show distinct crystallographic alignments. On a vicinal Ge surface with partially covered hBN grains, the atomic steps beneath the triangular-shaped hBN grains remain intact, as can be clearly seen in the AFM phase images (Figure 1e,f). Notably, on either substrate, each triangular hBN grain has an edge along the step direction. On Sub(A), the apex of most triangular hBN grains predominantly points toward the miscut direction, while, on Sub(B), they point either parallel or antiparallel to the miscut direction with a similar ratio (see Figure S4, Supporting Information, for scanning electron microscopy (SEM) images and the statistical distribution of grain orientations). Low-energy electron diffraction (LEED) measurements (Figure 1g,h) reveal a single hexagonal pattern of hBN, highlighted in a sapphire blue circle, that shares the same orientation as the pattern of the underlying Ge substrate, highlighted in a dotted red circle. This indicates that all the hBN grains have one zigzag edge along

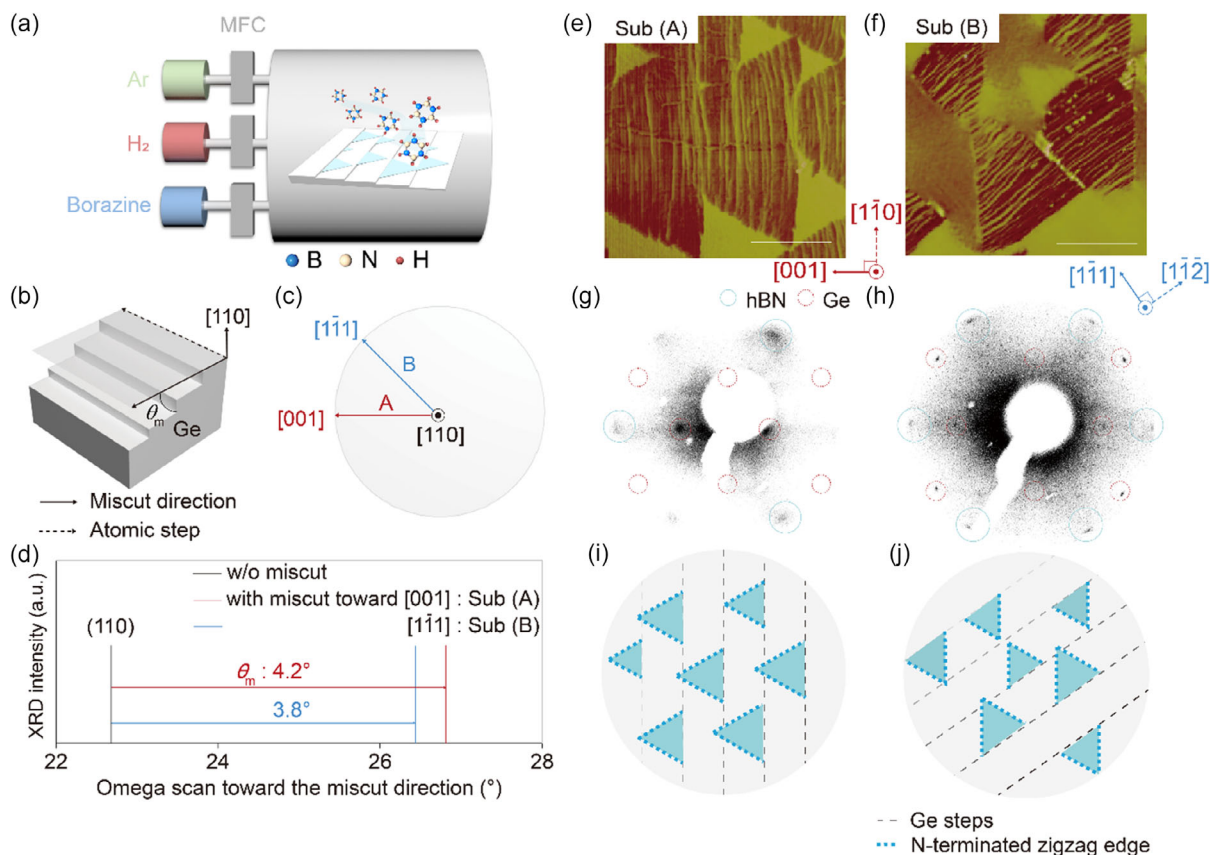


**Figure 1.** Epitaxial relationship between hBN and atomic steps of Ge. a,b) Schematic of the hBN growth setup and a miscut Ge(110) wafer, where the surface is tilted toward the miscut direction by angle  $\theta_m$  with respect to the (110) plane. c) Top view of a miscut Ge(110) wafer with miscut directions [001] for Sub(A) and  $[1\bar{1}\bar{1}]$  for Sub(B). d) XRD rocking curve for Ge(110) wafers without miscut and with miscut toward different directions. e,f) AFM phase images of partially grown ML hBN on Sub(A) and Sub(B), respectively. (Scale bar: 1  $\mu\text{m}$ ) g,h) LEED patterns of the samples on Sub(A) and Sub(B) over an area of 1  $\text{mm}^2$ . i,j) Schematics of partially grown hBN on miscut Ge(110). Two hBN edges not aligned with the Ge steps (marked as dotted black lines) are N-terminated zigzag edges (indicated by dotted sky blue lines) on both Sub(A) and Sub(B).

the  $[1\bar{1}\bar{0}]$  direction of Ge substrates on both substrates. The six diffraction spots of hBN on Sub(B) have nearly identical intensities, indicating the formation of both antiparallel hBN grains on Sub(B); in contrast, the pattern of hBN on Sub(A) is clearly asymmetric, suggesting that hBN grains on Sub(A) tend to align along one direction. (Figure 1i,j)

Considering that the interactions between the Ge steps and nucleated hBN edges contribute to the unidirectional growth of hBN by breaking the surface symmetry, the results in Figure 1 indicate that the interaction strength is stronger on Sub(A) than on Sub(B). It is known that Ge forms strong bonds with nitrogen,<sup>[19]</sup> leading the edges of hBN grains with dangling bonds to form Ge–N bonds to minimize their total free energy. LEED patterns on both Sub(A) and Sub(B) indicate that the zigzag edges of hBN are aligned with the  $[1\bar{1}\bar{0}]$  direction of Ge (Figure S5, Supporting Information) AFM phase images reveal that all the vertices of triangular hBN grains on Sub(A) have interior angles of  $60^\circ$ , with one edge parallel to the Ge atomic steps in the  $[1\bar{1}\bar{0}]$  direction (Figure S5b, Supporting Information), indicating that all the hBN edges are N-terminated zigzag edges (Figure 1i). In contrast, while the hBN grains on

Sub(B) have one edge parallel to the  $[1\bar{1}\bar{0}]$  direction of Ge, only one vertex has an interior angle of  $60^\circ$  (Figure S5c, Supporting Information), resulting in a non-N-terminated zigzag edge, aligned to the Ge atomic steps (Figure 1j). Geometric analysis (Figure S6, Supporting Information) indicates that the bond strength between the hBN edges and the Ge steps is indeed greater on Sub(A) than on Sub(B), due to the higher density of Ge atoms with dangling bonds along the step (Sub(A):  $0.25 \text{ nm}^{-1}$ , Sub(B):  $0.21 \text{ nm}^{-1}$ ). This is consistent with our observations, and the prediction is further confirmed quantitatively with subsequent simulations.

## 2.2. Effect of Hydrogen Partial Pressure on the Crystallographic Alignment of hBN

We studied how the crystallographic orientations of hBN depend on growth conditions, particularly the hydrogen partial pressure ( $P_{\text{H}_2}$ ), during the CVD process. On the same surface of Sub(A), hBN crystals were partially grown by modulating  $P_{\text{H}_2}$ , while the total growth pressure was kept constant at 760 Torr with the addition of argon flows. Most of the hBN grains form regular

triangles with one edge parallel to the Ge step edge. However, the apex between the other two edges points either downward along the Ge terrace, parallel to the miscut direction, or upward on the terrace, antiparallel to the miscut direction. These are marked as points of red and sapphire color in the schematic and SEM images in Figure 2a,b, respectively. The probability of the former type, denoted as  $\chi_{\text{align}}$ , increases with  $P_{\text{H}_2}$ , reaching nearly unity at  $P_{\text{H}_2} = 0.2$ , and then decreases again (refer to Figure S7, Supporting Information, for the probability distribution as a function of  $P_{\text{H}_2}$ ). Considering the same type of edge configuration for the triangular grains,  $\chi_{\text{align}}$  is correlated with the crystallographic alignment of hBN. Indeed, LEED patterns from samples with  $\chi_{\text{align}}$  values of  $\approx 0.5$  and 1 exhibit sixfold and threefold symmetrical intensity plots, respectively (see Figure 2c,d). This implies that there is growth of hBN with unidirectionally aligned crystallography in the sample with  $\chi_{\text{align}} \approx 1$ , at the optimum  $P_{\text{H}_2}$  value, denoted as  $P_{\text{opt,H}_2}$ .<sup>[9]</sup>

### 2.3. Wafer-Scale Formations of Single-Crystalline hBN

The formation of continuous hBN films by merging unidirectionally aligned grains can be scalable over wafer-scale. To observe the formation process of the single-crystalline hBN film, we conducted SEM imaging on as-grown samples on Ge(110) substrates with a miscut toward [001] after different growth times of 4, 8, and 12 h under the optimal growth condition (Figure 3a,b). The image contrast between the bare Ge and hBN-covered regions was significant, allowing us to clearly observe the merging of unidirectionally aligned triangular grains into a continuous film over time. At a surface coverage exceeding 80% (Figure 3b), triangular voids aligned in the same direction were formed, indicating that the crystallographic orientations of the hBN grains were maintained throughout the entire film formation process. The film exhibited a uniform contrast, indicating a consistent ML thickness. We note that the line features

with bright contrast, seen in Figure 3b, are wrinkles and are not associated with grain boundaries (Figure S8, Supporting Information).

The uniform growth of ML hBN with aligned crystallinity is scalable, resulting in a continuous film over a 2 inch Ge(110) substrate (Figure 3c and S9, Supporting Information). The hBN film transferred onto fused silica (Figure 3c, inset) showed similar optical transmission contrast spectra,  $1 - T$  at each measurement point across the entire film, which is consistent with those for ML hBN.<sup>[20]</sup> Here,  $T$  is defined as  $I/I_0$ , with  $I_0$  and  $I$  representing the transmission intensity through the bare substrate and the intensity through the substrate with the film, respectively.

To further characterize the hBN film, we conducted optical second harmonic generation (SHG) measurements. The SHG signals were measured from the hBN film transferred onto a SiO<sub>2</sub>/Si substrate in reflection mode using an excitation laser with a fundamental wavelength of 800 nm. The polarization-dependent SHG plot (Figure 3d) was measured with a parallel-aligned linear polarizer and analyzer while changing the relative orientation,  $\Phi$  of the polarization with respect to the sample. The SHG intensities show a sixfold symmetry, fitted as  $\cos^2(3\Phi)$ , representing the aligned crystallographic orientation of hBN.<sup>[21]</sup> Additionally, the SHG map (Figure 3e) shows uniform intensity, suggesting a lack of grain boundaries, where SHG is suppressed by destructive phase interference,<sup>[22]</sup> and multilayer regions with different stacking orders.<sup>[23]</sup>

### 2.4. DFT Calculations of Binding Energy Between hBN and Ge

We conducted DFT calculations to understand how the hBN grains are aligned with respect to the Ge epilayer (Figure 4a). Unlike metallic substrates for epitaxial hBN growth,<sup>[8–14]</sup> the Ge surface might be passivated by hydrogen atoms. At high  $P_{\text{H}_2}$ , both hBN edges and Ge surface are expected to be hydrogen-passivated (Figure 4b). Our DFT calculations show that, at

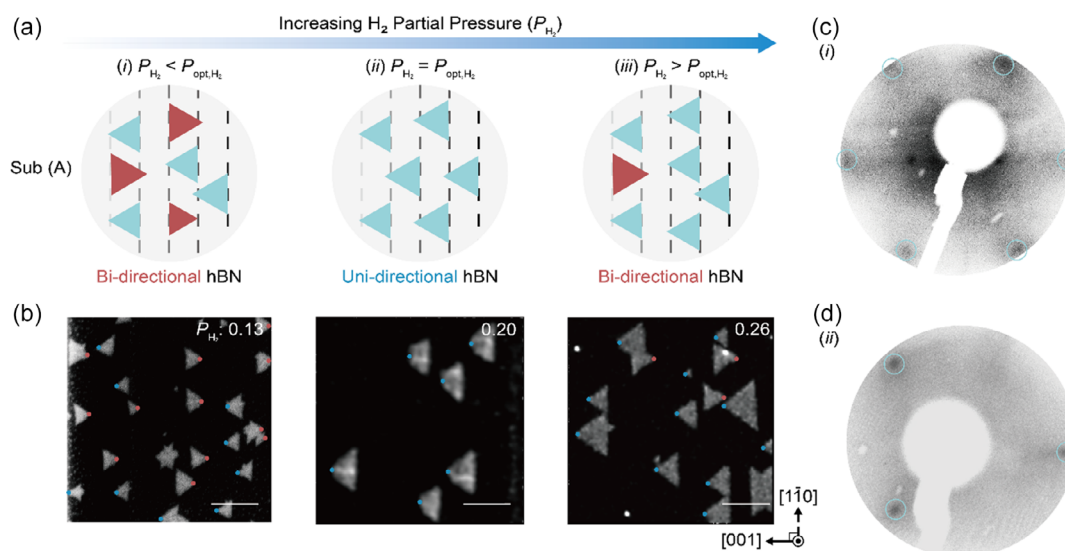


**Figure 2.** Effect of hydrogen partial pressure on the crystallographic alignment of hBN. a) Schematic illustration of the variation in the degree of hBN alignment as  $P_{\text{H}_2}$  increases. b) SEM images of hBN grains with increasing  $P_{\text{H}_2}$ . (Scale bar: 1  $\mu\text{m}$ ) c,d) LEED patterns of (c) hBN film with bidirectional crystal growth and (d) unidirectional crystal growth.

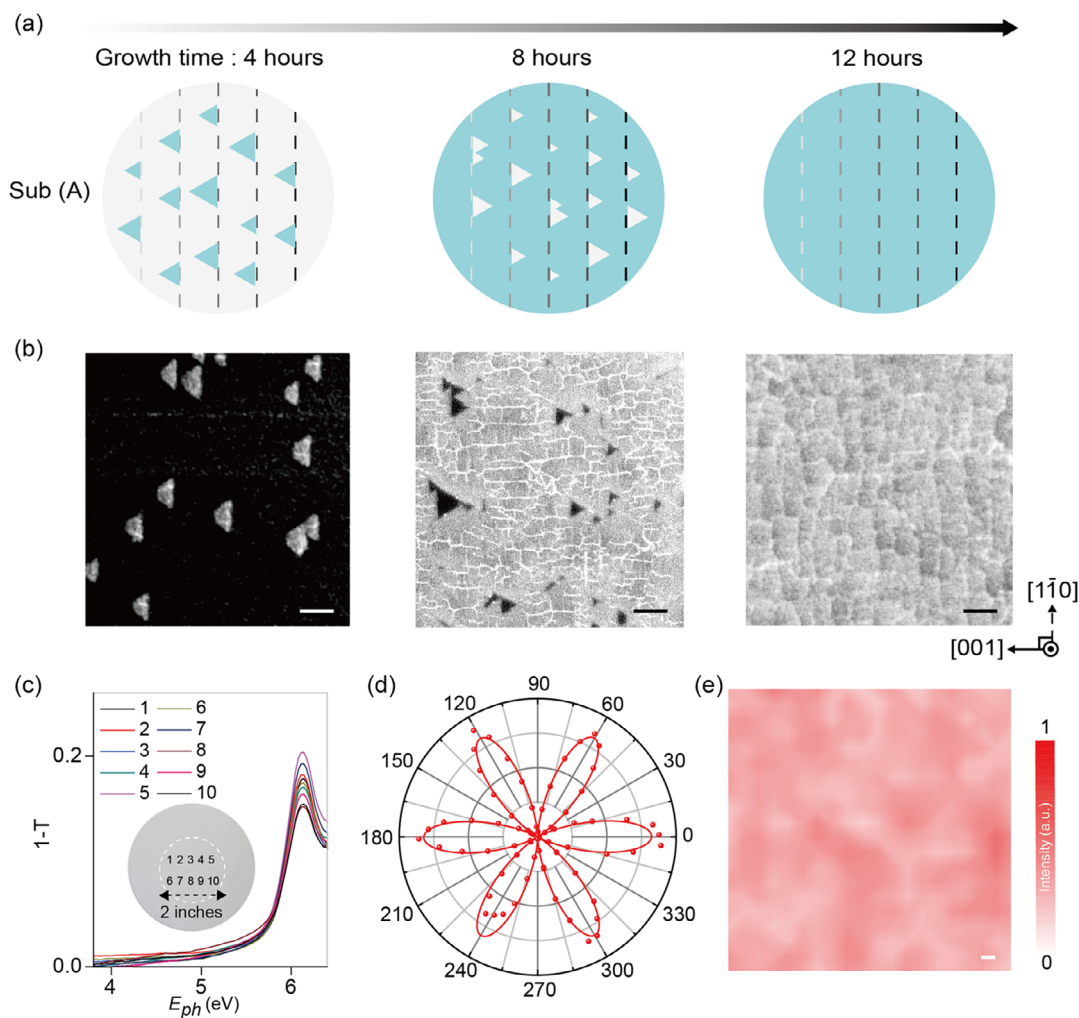


**Figure 3.** Wafer-scale formations of single-crystalline hBN. a) Schematic of the sequential process of hBN film formation through the merging of unidirectional grains on Ge(110) substrates with a miscut. b) SEM images of as-grown hBN samples at different growth times (4, 8, and 12 h from left to right). c) Optical transmission contrast spectra measured at the positions indicated in the inset (inset: the hBN film transferred onto fused silica, with the hBN film region highlighted by a dotted line). d) Polar plot of the SHG intensity as a function of the crystal's azimuthal angle  $\Phi$ . e) SHG intensity map. Scale bar: 1  $\mu\text{m}$ .

the edge of hBN, the nitrogen–hydrogen (N–H) bonding strength is 5.34 eV per bond, which is significantly higher than that of Ge–hydrogen bonds (Ge–H) on Ge(110) surface, 3.11 eV per bond. Therefore, hBN edges are more likely to be hydrogen-passivated than the Ge surface. To understand the epitaxial growth behavior of hBN on Ge(110), we calculated the binding energies ( $E_B$ ) of a hBN island on both Ge(110) surface with and without hydrogen passivation. The calculated binding energies of hBN with different orientation angles are shown in Figure 4c, from which we can clearly see two local minima at  $\theta = 0^\circ$  and  $60^\circ$  for both curves. For each case, the  $E_B$  at  $\theta = 0^\circ$  and  $60^\circ$  are very close to each other. The tiny energy difference of less than 0.01 eV made the orientations of  $\theta = 0^\circ$  and  $60^\circ$  undistinguishable, which explains that the hBN islands grown on Ge(110) terrace generally have two orientations. In contrast, the energy barrier of rotating the hBN island on pristine Ge(110) surface is  $\approx 0.78$  eV, which is more than one order

of magnitude larger than that on the hydrogen-passivated Ge(110) surface, which is only about 0.046 eV.

It is known that introducing atomic steps on a flat terrace may lead to unidirectional alignments of 2D islands due to the strong interaction between the step edge and the hBN edge. So, we further considered the binding energy between the hBN edge and the step edge of the Ge(110) surface. At a high hydrogen pressure, both the hBN edge and the whole Ge(110) surface are terminated by hydrogen and, therefore, the interaction between the hydrogen-terminated hBN edge and the hydrogen-passivated Ge(110) surface is of the weak vdW-type. As shown in Figure 4d, the weak step edge–hBN edge interaction only leads to a very shallow energy minimum in the  $E_B$  versus  $\theta$  curve at  $\theta = 0^\circ$  and  $E_B$  at  $\theta = 60^\circ$  is a local minimum. Consequently, both hBN domains with  $\theta = 0^\circ$  and  $60^\circ$  are of very similar stabilities. This result is in agreement with our observations of hBN bicrystal grown at high  $P_{H_2}$ .

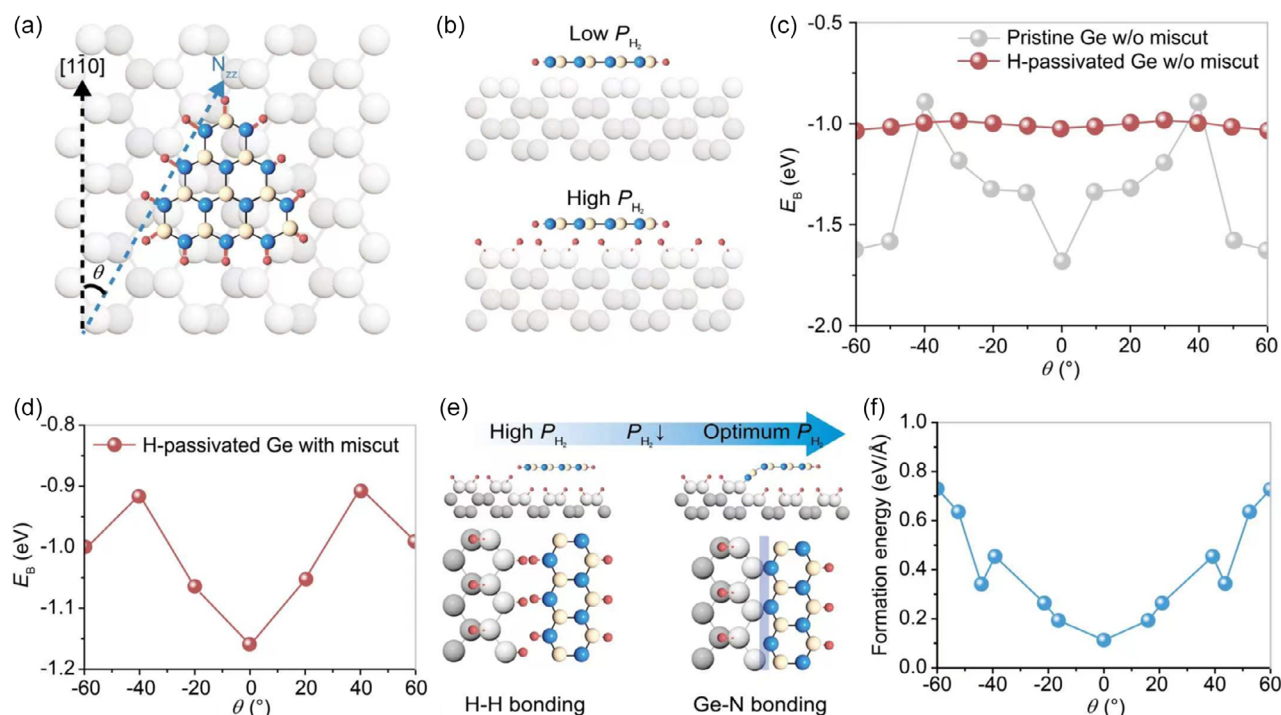


**Figure 4.** DFT calculations of binding energy between hBN and Ge. a) Schematics of an hBN grain with N-terminated zigzag edges on Ge(110). The angle ( $\theta$ ) indicates the misorientation between the hBN edge and the Ge  $[1\bar{1}0]$  direction. b) Schematics of the side view of hBN on (top) pristine Ge(110) and (bottom) hydrogen-passivated Ge(110). c) Binding energy between hBN and Ge(110) (gray) without hydrogen passivation and (red) with hydrogen passivation as a function of  $\theta$ . d) Binding energy between hBN and hydrogen-passivated Ge(110) with a miscut as a function of  $\theta$ . e) Schematic illustration of bond formation between a Ge atomic step and hBN at different  $P_{H_2}$ . f) Formation energy for one-dimensional hBN/Ge step interfaces as a function of  $\theta$ , when hBN and Ge form direct chemical bonds without hydrogen passivation.

As shown in Figure S10, Supporting Information, at a reduced hydrogen pressure (or a lower chemical potential of hydrogen), direct chemical bonds between the Ge step edge and the hBN edge (as shown in Figure 4e) are energetically favorable. We calculated the formation energy of the Ge step edge-hBN interface as a function of  $\theta$  and the result is shown in Figure 4f, from which we can see that  $\theta = 0^\circ$  corresponds to a deep global minimum of the formation energy curve and  $\theta = 60^\circ$  corresponds to a global maximum. Therefore, at an intermediate  $P_{H_2}$ , which is sufficient to passivate both the Ge substrate and the hBN edge but also allows the formation of Ge-N bonds between the hBN edge and the Ge step edge, step-directed unidirectional growth of hBN can be achieved. The simulation results are consistent with the experimentally observed nonmonotonic change of  $\chi_{align}$  as a function of  $P_{H_2}$ .

## 2.5. Applications of Single-Crystalline hBN Films

The fact that Ge surfaces can be hydrogen-passivated makes them unique compared to other epitaxial metal substrates used for growing unidirectional hBN.<sup>[18]</sup> Due to the hydrogen passivation, the hBN films can be mechanically exfoliated and assembled to form atomically clean vdW interfaces without exposure to other chemicals, as shown in Figure 5a. Angle-resolved photoemission spectroscopy (ARPES) data, conducted on a few-hundred-micrometer-wide region of the as-grown ML hBN film,

reveal clear bands expected for hBN with aligned crystallography (see Figure 5b). Using these films, we have fabricated an hBN bilayer by layer-by-layer assembly with aligned crystallography. The ARPES data (Figure 5c) demonstrate clear band splitting along the  $\Gamma$ -K momentum direction attributed to interlayer  $P_z$  orbital hybridization,<sup>[24]</sup> confirming that the fabricated interfaces are pristine. Since the hBN assembly units possess unidirectional crystallinity, we can further control the stacking order of the hBN bilayers, which significantly affects their electrical and optical properties.<sup>[25–29]</sup> For demonstration, we assembled two ML hBN films with the crystallographic alignment either parallel or antiparallel. The diffraction patterns from transmission electron microscopy reveal a single hexagonal pattern for the bilayer samples with different stacking orders, indicating precise alignment (Figure 5d,e). However, the relative intensity ratios between the inner and outer spots differ, as shown in the insets of Figure 5d,e, which are consistent with targeted rhombohedral and hexagonal stacking orders, respectively.<sup>[23]</sup> Although a slight misorientation angle from the targeted alignment ( $<1^\circ$ ) may occur during assembly, atomic reconstruction tends to yield stable atomic configurations with overlapping elements of opposite charge polarities (i.e., boron on nitrogen, or nitrogen on boron).<sup>[23]</sup> We note that the rhombohedral stacking order, with its distinct crystal symmetry (noncentrosymmetric, lacking a mirror plane parallel to the layer), results in emergent properties such as ferroelectricity and nonlinear optical characteristics.

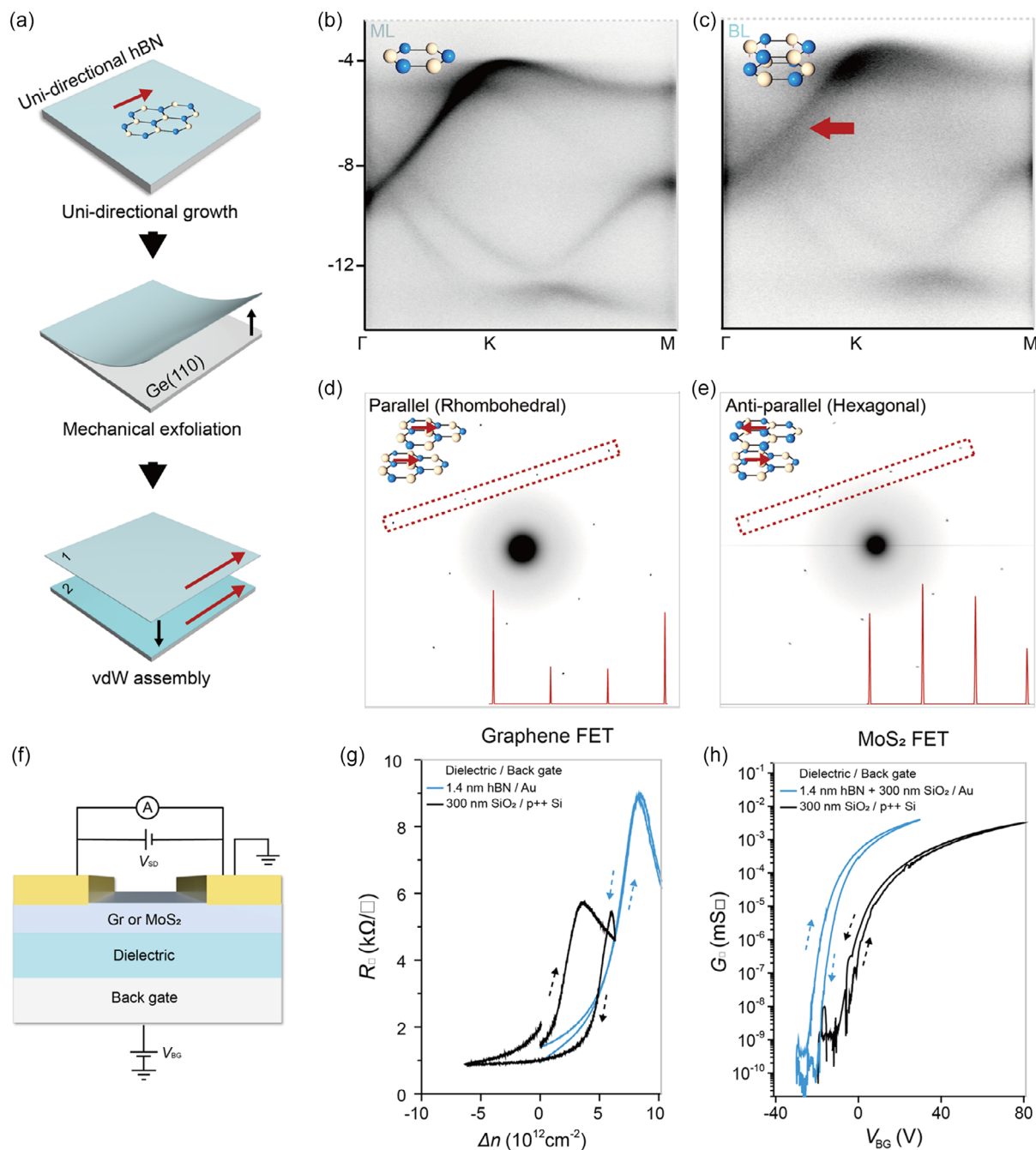


**Figure 5.** Applications of single-crystalline hBN films. a) Schematic illustration of the layer-by-layer assembly process. b,c) ARPES data for (b) as-grown ML and (c) assembled bilayer hBN films. In the assembled bilayer hBN, band splitting (indicated by a red arrow) occurs along the  $\Gamma$ -K direction, representing effective interlayer coupling. d,e) TEM diffraction patterns of bilayer hBN assembled with (d) parallel and (e) antiparallel interlayer alignment of crystallography. f) Schematic of Gr and MoS<sub>2</sub> FET devices. g,h) (g) Sheet resistance versus  $V_{BG}$  for Gr FETs, and (h) sheet conductance versus applied gate for MoS<sub>2</sub> FETs with different dielectrics.

Despite significant interest, producing this metastable phase on a large-scale has been challenging. Our layer-by-layer assembly of unidirectionally grown films now provides a method for fabricating this film.

We also fabricated graphene (Gr) and MoS<sub>2</sub>-based FETs using the hBN film as a dielectric interlayer (Figure 5f).

(see Experimental Section for the details) Electrical transport in the Gr FETs was compared between hBN and SiO<sub>2</sub> dielectric. In the sheet resistance ( $R_{\square}$ ) versus applied gate,  $V_{BG}$  curves, measured with a sweep rate for field-induced carrier density of  $3 \times 10^{10} \text{ cm}^{-2} \text{ s}^{-1}$  (Figure 5g), we observed significant suppression of hysteresis with the hBN dielectric, implying

effectively suppressed interfacial traps. To quantify the interfacial trap densities, we deduced the change of surface carrier concentration,  $\Delta n$ , induced by  $V_{BG}$ . Here,  $\Delta n = V_{BG} C_g / e$ , where  $C_g$  is the gate capacitance per unit area, and  $e$  is the elementary charge. The difference in  $\Delta n$  at the charge neutrality points for the forward and reverse sweeps indicates the trap density. The reduced density is lowered to  $3.50 \times 10^{11} \text{ cm}^{-2}$  with hBN dielectric from  $3.48 \times 10^{12} \text{ cm}^{-2}$  with  $\text{SiO}_2$  dielectric, representing a reduction by roughly an order of magnitude. The graphene field-effect mobility,  $\mu$ , was also extracted by fitting the transconductance curves with  $\mu = dG_{\square} / d\Delta n \cdot (1/e)$  based on the Drude model, where  $G_{\square}$  indicates sheet conductance. As a result,  $\mu$  for electrons and holes are 108 and  $1394 \text{ cm}^2 \text{ V}^{-1} \text{ s}$  for  $\text{SiO}_2$  dielectrics, and 207 and  $723 \text{ cm}^2 \text{ V}^{-1} \text{ s}$  for hBN dielectrics. We suspect that Coulomb interactions through the ultrathin hBN dielectric of  $\approx 1.4 \text{ nm}$  between the channel and the gate affected the field-effect mobility. Nonetheless, the significant suppression of hysteresis in the transconductance sweep was evident, indicating a reduction of trap states in the dielectric compared to silicon oxides.<sup>[30]</sup>

In  $\text{MoS}_2$  FET, we compared the subthreshold swing (SS) and mobility ( $\mu$ ) from transconductance curves with and without the hBN interlayer on a  $\text{SiO}_2/\text{Si}$  substrate (Figure 5h). The introduction of hBN increases  $\mu$  from 12 to  $15.8 \text{ cm}^2 \text{ V}^{-1} \text{ s}^{-1}$  and decreases the SS from 2.3 to  $1.2 \text{ V dec}^{-1}$ . The SS can be expressed as  $\ln(10) \cdot V_{th} \cdot \{1 + (C_{ch} + eD_{it}) / C_{ins}\}$ , where  $V_{th}$  is the thermal voltage,  $C_{ch}$  is the channel capacitance,  $D_{it}$  is the density of interface states, and  $C_{ins}$  is the insulator capacitance.<sup>[31]</sup> The difference in the deduced  $D_{it}$  with and without hBN is estimated to be  $8.27 \times 10^{11} \text{ cm}^{-2} \text{ eV}^{-1}$ .

### 3. Conclusion

In conclusion, we have grown large-scale hBN ML films with unidirectional crystallography on miscut Ge(110) substrates using CVD. Our experimental and theoretical studies suggest that Ge step-assisted epitaxy thermodynamically determines the orientation of hBN grains when the  $P_{\text{H}_2}$  during growth is optimized to passivate the Ge terrace, while still allowing direct bonding between hBN grains and the Ge steps at the nucleation stages. For the first time, the unidirectional hBN ML films were mechanically exfoliated from the growth substrates for atomically clean assembly, implying that this process can be useful for fabricating multilayered hBN with controlled stacking orders, and for creating advanced electronic and optoelectronic devices using vdW materials.<sup>[32–34]</sup>

### 4. Experimental Section

**Growth of hBN:** Ge (110) substrates miscut by  $4^\circ$  toward [001] or  $[1\bar{1}0]$  (PAM-XIAMEN) were cleaned in 20% HF solution for 3 min to remove native oxides. The Ge substrates were then loaded into a quartz tube, which was evacuated to 40 mTorr and subsequently refilled to atmospheric pressure with combinations of 99.99%  $\text{H}_2$  and 99.99% Ar. The tube was annealed until it reached  $930^\circ \text{C}$  over 1 h, with various ratios of  $\text{H}_2$  to Ar (At the optimum hydrogen partial pressure for unidirectional growth, 4000 sccm of Ar and 1000 sccm of  $\text{H}_2$  were used). Borazine (Gelest-INB0009) was then introduced for 12 h using Ar as a carrier gas (0.3 sccm) to grow a unidirectional ML hBN film. After the growth of

hBN, the borazine flow was turned off and the furnace was opened to cool naturally.

**Characterizations:** All LEED patterns were obtained over an area of  $\approx 1 \text{ mm}^2$ , using an optics system (ErLEED 150) at 98 eV and  $10^{-9}$  Torr. XRD patterns of vicinal Ge substrates were acquired using an X-ray diffractometer (Empyrean, Panalytical) with Cu K $\alpha$  radiation. The hBN domains were observed using a high-resolution field-emission SEM (Hitachi S-4800) by detecting secondary electrons from hBN/Ge surface. Band structures of hBN were investigated at the 10D beamline at the Pohang Accelerator Laboratory using an electron analyzer (Scienta DA30) with a photon energy of 55 eV. Additionally, hBN films were transferred onto a SiN TEM grid (EMS, 76042-48) for diffraction pattern analysis and dark field imaging at 200 keV using a transmission electron microscope (Jeol, JEM-2100 F).

**Layer-by-Layer Assembly:** An Au layer was deposited to 40 nm thickness on a hBN/Ge(110) sample. Then, polymethyl methacrylate (PMMA, 996 K, 8% in anisole) was spin-coated onto the Au film at 1500 rpm for 15 s, then annealed at  $190^\circ \text{C}$  for 15 min on a hot plate. A thermal-release tape (TRT, Nitto 3195HS) was attached to the top of the PMMA/Au/hBN/Ge(110) sample as a handling layer to enable mechanical exfoliation of TRT/PMMA/Au/hBN. Then the exfoliated TRT/PMMA/Au/hBN film was attached to another as-grown hBN on Ge(110) sample with controlled stacking orientation and baked at  $180^\circ \text{C}$  for 10 min to increase the mechanical-exfoliation yield. By repeating the assembly process with different twist angles, we can control the stacking order and the total number of layers in the final films (Figure S11a, Supporting Information). Finally, the Au film was etched with  $\text{KI}/\text{I}_2$  solution, and the surface was rinsed with ethanol and deionized (DI) water. The pristine interfaces of the assembled hBN multilayers were confirmed by XRD (Figure S11b, Supporting Information). Please refer to our previous report<sup>[18]</sup> for more details.

**Computational Details:** All the DFT calculations were performed using the Vienna Ab initio Simulation Package (VASP).<sup>[35,36]</sup> The generalized gradient approximation and projected augmented wave method were used to describe the exchange-correlation functions and the interaction between electrons and ion cores. The plane wave cutoff energy was set as 300 eV, and  $1 \times 1 \times 1$  k-point meshes were adopted for these DFT calculations. The convergence criteria of the forces and energies were set to be  $0.02 \text{ eV \AA}^{-1}$  and  $1.0 \times 10^{-4} \text{ eV}$ , respectively. A vacuum layer with a thickness of greater than  $15 \text{ \AA}$  was used to avoid the interactions between two neighboring images. The vdW interactions were corrected by the DFT-D3.<sup>[37]</sup> We constructed a model of ML hBN domain on a three-layer Ge substrates with the bottom layer fixed and hydrogen-passivated. The binding energy ( $E_B$ ) and formation energy ( $E_f$ ) are calculated using the following two equations

$$E_B = (E_{\text{total}} - E_{\text{Ge}} - E_{\text{hbn}}) / A \quad (1)$$

$$E_f = (E_{\text{total}} - E_{\text{Ge}} - E_{\text{hbn}} + \epsilon_{\text{pri}}) / L \quad (2)$$

where  $E_{\text{total}}$ ,  $E_{\text{Ge}}$ , and  $E_{\text{hbn}}$  are the energies of the whole system, the Ge substrate and the hBN layer, respectively.  $A$  is the area of the hBN domain.  $L$  is the length of the supercell of the hBN/Ge(110) system.  $\epsilon_{\text{pri}}$  is the formation energy of hBN with a free edge, which is referred to our previous study.<sup>[10]</sup> To compare the free-energy difference between Ge–H and the Ge–N edges, two atomic configurations are modeled: both hBN and a stepped Ge(110) surface with H-passivated (Figure S10,i, Supporting Information) and the model with one H removed from hBN and Ge(110) surface (Figure S10, ii, Supporting Information), respectively. The free energy for the aforementioned models can be calculated using the following equations

$$G_i = (E_{\text{total}} - E_{\text{Ge}} - E_{\text{hbn}}) - 0.5n_{\text{H}}(E_{\text{H}_2} + \Delta\mu_{\text{H}_2}) \quad (3)$$

$$G_{ii} = (E_{\text{total}} - E_{\text{Ge}} - E_{\text{hbn}}) - 0.5(n_{\text{H}} - 2)(E_{\text{H}_2} + \Delta\mu_{\text{H}_2}) \quad (4)$$

where  $E_{\text{total}}$ ,  $E_{\text{Ge}}$ ,  $E_{\text{hbn}}$ ,  $n_{\text{H}}$ ,  $E_{\text{H}_2}$ , and  $\Delta\mu_{\text{H}_2}$  represent the total energy of the supercell, the energy of the Ge substrate, the energy of the hBN domain, the number of hydrogen atoms at the hBN edge, and the energy of a hydrogen molecule ( $-6.7617 \text{ eV molecule}^{-1}$ ), and the chemical potential of



hydrogen, respectively. The free energies as a function of H<sub>2</sub> chemical potential for the aforementioned models were further calculated in Figure S10, Supporting Information.

**Device Fabrications:** Four- to five-layer hBN films were first fabricated onto a Ge substrate using a layer-by-layer assembly method. This assembled 4 layers of hBN was subsequently transferred onto a Si substrate for Gr FETs, and 5 layers were transferred onto a SiO<sub>2</sub>/Si substrate for MoS<sub>2</sub> FETs. Then, Gr or MoS<sub>2</sub> was transferred onto the hBN films. Metal electrodes, Cr/Au (15/40 nm) for Gr FETs and Bi/Au (15/40 nm) for MoS<sub>2</sub> FETs, were deposited using a thermal evaporator and patterned by photolithography.

## Supporting Information

Supporting Information is available from the Wiley Online Library or from the author.

## Acknowledgements

This research was supported by the National R&D Program through the National Research Foundation of Korea (NRF) funded by the Ministry of Science and ICT (RS-2023-00234622, 2023R1A2C2005427, RS-2023-00258309) and the Institute for Basic Science (IBS-R034-D1).

## Conflict of Interest

The authors declare no conflict of interest.

## Author Contributions

**Ju-Hyun Jung** and **Cheol-Joo Kim** designed the experiments. **Ju-Hyun Jung** synthesized the hBN samples. **Chao Zhao** and **Feng Ding** performed the DFT calculations. **Ju-Hyun Jung**, **Seong-Jun Yang**, **Jun-Ho Park**, and **Chan-Cuk Hwang** conducted the structural characterizations on hBN, including TEM and LEED. **Seong-Jun Yang** and **Woo-Ju Lee** fabricated and characterized the electronic devices. **Su-Beom Song** and **Jonghwan Kim** conducted optical second harmonic generation and analyses. **Seung-Hwa Baek** conducted XPS and FTIR analyses on hBN. **Ju-Hyun Jung** and **Cheol-Joo Kim** wrote the manuscript with input from all authors. **Ju-Hyun Jung** and **Chao Zhao** contributed equally to this work.

## Data Availability Statement

The data that support the findings of this study are available in the supplementary material of this article.

## Keywords

chemical vapor deposition, epitaxy, hexagonal boron nitride, hydrogen passivations, single crystal, van der Waals assembly

Received: June 11, 2024

Revised: September 26, 2024

Published online:

[1] J. Wang, Q. Yao, C. W. Huang, X. Zou, L. Liao, S. Chen, Z. Fan, K. Zhang, W. Wu, X. Xiao, *Adv. Mater.* **2016**, *28*, 8302.

[2] X.-X. Li, Z.-Q. Fan, P.-Z. Liu, M.-L. Chen, X. Liu, C.-K. Jia, D.-M. Sun, X.-W. Jiang, Z. Han, V. Bouchiat, *Nat. Commun.* **2017**, *8*, 970.

- [3] J.-H. Park, S.-J. Yang, C.-W. Choi, S.-Y. Choi, C.-J. Kim, *ACS Appl. Mater. Interfaces* **2021**, *13*, 22828.
- [4] M. Farmanbar, G. Brocks, *Adv. Electron. Mater.* **2016**, *2*, 1500405.
- [5] J. I. Wang, M. A. Yamoah, Q. Li, A. H. Karamlou, T. Dinh, B. Kannan, J. Braumüller, D. Kim, A. J. Melville, S. E. Muschinske, *Nat. Mater.* **2022**, *21*, 398.
- [6] A. Mishchenko, J. Tu, Y. Cao, R. V. Gorbachev, J. Wallbank, M. Greenaway, V. Morozov, S. Morozov, M. Zhu, S. Wong, *Nat. Nanotechnol.* **2014**, *9*, 808.
- [7] L. Ma, P. X. Nguyen, Z. Wang, Y. Zeng, K. Watanabe, T. Taniguchi, A. H. MacDonald, K. F. Mak, J. Shan, *Nature* **2021**, *598*, 585.
- [8] Q. Zhang, H. Chen, S. Liu, Y. Yu, C. Wang, J. Han, G. Shao, Z. Yao, *Nanoscale* **2022**, *14*, 3112.
- [9] L. Wang, X. Xu, L. Zhang, R. Qiao, M. Wu, Z. Wang, S. Zhang, J. Liang, Z. Zhang, *Nature* **2019**, *570*, 91.
- [10] T.-A. Chen, C.-P. Chuu, C.-C. Tseng, C.-K. Wen, H.-S. P. Wong, S. Pan, R. Li, T.-A. Chao, W.-C. Chueh, Y. Zhang, *Nature* **2020**, *579*, 219.
- [11] J. Li, Y. Li, J. Yin, X. Ren, X. Liu, C. Jin, W. Guo, *Small* **2016**, *12*, 3645.
- [12] K. Y. Ma, L. Zhang, S. Jin, Y. Wang, S. I. Yoon, H. Hwang, J. Oh, D. S. Jeong, M. Wang, S. Chatterjee, *Nature* **2022**, *606*, 88.
- [13] J. Dong, L. Zhang, X. Dai, F. Ding, *Nat. Commun.* **2020**, *11*, 5862.
- [14] J. S. Lee, S. H. Choi, S. J. Yun, Y. I. Kim, S. Boandoh, J.-H. Park, B. G. Shin, H. Ko, S. H. Lee, Y.-M. Kim, Y. H. Lee, K. K. Kim, S. M. Kim, *Science* **2018**, *362*, 817.
- [15] K. V. Bets, N. Gupta, B. I. Yakobson, *Nano Lett.* **2019**, *19*, 2027.
- [16] M. T. Greenaway, E. Vdovin, D. Ghazaryan, A. Misra, A. Mishchenko, Y. Cao, Z. Wang, J. Wallbank, M. Holwill, Y. N. Khanin, *Commun. Phys.* **2018**, *1*, 94.
- [17] H. J. Park, J. Cha, M. Choi, J. H. Kim, R. Y. Tay, E. H. T. Teo, N. Park, S. Hong, Z. Lee, *Sci. Adv.* **2020**, *6*, eaay4958.
- [18] S.-J. Yang, J.-H. Jung, E. Lee, E. Han, M.-Y. Choi, D. Jung, S. Choi, J.-H. Park, D. Oh, S. Noh, *Nano Lett.* **2022**, *22*, 1518.
- [19] J. Yin, X. Liu, W. Lu, J. Li, Y. Cao, Y. Li, Y. Xu, X. Li, J. Zhou, C. Jin, *Small* **2015**, *11*, 5375.
- [20] R. W. Havener, C.-J. Kim, L. Brown, J. W. Kevek, J. D. Sleppy, P. L. McEuen, J. Park, *Nano Lett.* **2013**, *13*, 3942.
- [21] Y. Li, Y. Rao, K. F. Mak, Y. You, S. Wang, C. R. Dean, T. F. Heinz, *Nano Lett.* **2013**, *13*, 3329.
- [22] J. Cheng, T. Jiang, Q. Ji, Y. Zhang, Z. Li, Y. Shan, X. Gong, W. Liu, S. Wu, *Adv. Mater.* **2015**, *27*, 4069.
- [23] C.-J. Kim, L. Brown, M. W. Graham, R. Hovden, R. W. Havener, P. L. McEuen, D. A. Muller, J. Park, *Nano Lett.* **2013**, *13*, 5660.
- [24] H. Henck, D. Pierucci, G. Fugallo, J. Avila, G. Cassabois, Y. J. Dappe, M. G. Silly, C. Chen, B. Gil, M. Gatti, *Phys. Rev. B* **2017**, *95*, 085410.
- [25] M. Vizner Stern, Y. Waschitz, W. Cao, I. Nevo, K. Watanabe, T. Taniguchi, E. Sela, M. Urbakh, O. Hod, M. Ben Shalom, *Science* **2021**, *372*, 1462.
- [26] M. Lv, J. Wang, M. Tian, N. Wan, W. Tong, C. Duan, J. Xue, *Nat. Commun.* **2024**, *15*, 295.
- [27] K. Yao, N. R. Finney, J. Zhang, S. L. Moore, L. Xian, N. Tancogne-Dejean, F. Liu, J. Ardelean, X. Xu, D. Halbertal, *Sci. Adv.* **2021**, *7*, eabe8691.
- [28] H. Y. Lee, M. M. Al Ezzi, N. Raghuvanshi, J. Y. Chung, K. Watanabe, T. Taniguchi, S. Garaj, S. Adam, S. Gradecak, *Nano Lett.* **2021**, *21*, 2832.
- [29] D. S. Kim, R. C. Dominguez, R. Mayorga-Luna, D. Ye, J. Embley, T. Tan, Y. Ni, Z. Liu, M. Ford, F. Y. Gao, *Nat. Mater.* **2024**, *23*, 65.
- [30] T. Knobloch, Y. Y. Illarionov, F. Ducry, C. Schleich, S. Wachter, K. Watanabe, T. Taniguchi, T. Mueller, M. Wältl, M. Lanza, *Nat. Electron.* **2021**, *4*, 98.
- [31] Y. Y. Illarionov, T. Knobloch, M. Jech, M. Lanza, D. Akinwande, M. I. Vexler, T. Mueller, M. C. Lemme, G. Fiori, F. Schwierz, *Nat. Commun.* **2020**, *11*, 3385.

- [32] C. Su, F. Zhang, S. Kahn, B. Shevitski, J. Jiang, C. Dai, A. Ungar, J.-H. Park, K. Watanabe, T. Taniguchi, *Nat. Mater.* **2022**, 21, 896.
- [33] K. Yasuda, X. Wang, K. Watanabe, T. Taniguchi, P. Jarillo-Herrero, *Science* **2021**, 372, 1458.
- [34] T. H. Yang, B.-W. Liang, H.-C. Hu, F.-X. Chen, S.-Z. Ho, W.-H. Chang, L. Yang, H.-C. Lo, T.-H. Kuo, J.-H. Chen, *Nat. Electron.* **2024**, 7, 29.
- [35] G. Kresse, J. Furthmüller, *Comput. Mater. Sci.* **1996**, 6, 15.
- [36] G. Kresse, J. Hafner, *Phys. Rev. B* **1993**, 48, 13115.
- [37] S. Grimme, J. Antony, S. Ehrlich, H. Krieg, *J. Chem. Phys.* **2010**, 132, 154104.